Received: 23 July 2020 | Revised: 4 January 2021 | Accepted: 2 February 2021

IET Microwaves, Antennas & Propagation

DOI: 10.1049/mia2.12115

The Institution of Engineering and Technology WILEY

ORIGINAL RESEARCH PAPER

Analysis of wave scattering from 2D curved metasurfaces using Floquet and Fourier series expansions

Maryam S. Khatami[1] | **Mojtaba Dehmollaian**[2,3] | **Leila Yousefi**[4,5]

[1]School of Electrical and Computer Engineering, University of Tehran, Tehran, Iran

[2]Center of Excellence on Applied Electromagnetic Systems, School of Electrical and Computer Engineering, University of Tehran, Tehran, Iran

[3]Department of Electrical Engineering, Polytechnique Montréal, Montreal, QC, Canada

[4]School of Electrical and Computer Engineering, Faculty of Engineering, University of Tehran, Tehran, Iran

[5]Department of Electrical and Computer Engineering, University of Waterloo, Waterloo, ON, Canada

Correspondence

Maryam S Khatami, School of Electrical and Computer Engineering, University of Tehran, Tehran, Iran.
Email: ma.khatami@ut.ac.ir

Abstract

An efficient technique for calculating the scattering from curved metasurfaces using the extinction theorem in conjunction with the Floquet and Fourier series expansions is presented. Here, we treat the two-dimensional metasurfaces that have transversal polarizabilities with no variation along the y-axis. The boundary conditions at the metasurface are given by the generalized sheet transition conditions (GSTCs) whose susceptibilities are given in an arbitrary local coordinate system. First, we use the extinction theorem to provide integral equations of the scattering problem. The integral equations involve the Green's functions, tangential electric and magnetic fields and their normal derivatives in regions above and below the metasurface. Then, we employ the Floquet theorem that gives us the analytical periodic Green's functions of each region. Next, we employ the Fourier theorem to expand the tangential fields in terms of unknown Fourier coefficients. The GSTCs and the integral equations provide equations to be solved for the unknowns. The method can calculate scattering from both periodic and non-periodic metasurfaces. The technique is used to analyse different applied problems such as carpet cloaking, illusion, and radar echo width reduction. The method is fast and accurate and can efficiently treat metasurfaces with electrically large curved geometries with dimensions as large as 120 times the wavelength.

1 | INTRODUCTION

Metasurfaces, two-dimensional (2D) version of metamaterials have advantages over volumetric, three-dimensional (3D) metamaterials. They are more convenient (lighter and easier to fabricate) and generally have lower loss [1–5]. They have been used in various applications such as cloaking [6, 7], illusion [8], radar cross-section (RCS) reduction, flat lens [9], thin-film solar cells [10, 11], far-field sub-wavelength and computational imaging [12–14] among several other applications.

Particularly, for the application of cloaking, several works were reported. A mantle cloak aims to make a free object coated by a metasurface invisible [15–21], while, a carpet cloak hides an object placed on the ground. Although piece-wise flat metasurfaces are more convenient [7–22], they result in unavoidable diffraction from the edges. Therefore, curved metasurfaces are advantageous for the application of cloaking.

Phase gradient metasurfaces, used for cloaking or illusion, are usually analysed using full-wave numerical methods [23, 24]. However, the full-wave numerical simulation of metacells is very time-consuming making it impractical to simulate electrically large structures. In another approach, we can replace the whole metasurface with a united and zero-thickness artificial boundary, modelled by the generalized sheet transition conditions (GSTCs) [25, 26]. Generalized Snell's law [6, 7] can be used to analyse a phase gradient metasurface, however, the GSTCs provide more wave transformations including various field magnitude, phase, and polarization in addition to the propagation direction.

A combination of numerical methods such as finite difference time domain technique [26–29] or finite element method (FEM) [30] with the GSTCs has been previously presented to analyse metasurfaces. However, these approaches generally consume a large amount of time to simulate electrically large

metasurfaces. Integral-equation-based methods acquire less run time when compared to other numerical techniques. However, previously reported integral-equation-based methods are limited to flat metasurfaces [31] and are not able to analyse curved metasurfaces [32].

Here, an efficient analytical method based on the extinction theorem integral equations is proposed to solve scattering from curved metasurfaces modelled by the GSTCs. It deals with 2D metasurfaces that have no variation in the y-direction and that have transversal polarizabilities. In the proposed approach, susceptibilities are defined in the local coordinate system, in contrast to some previous researches [27, 33] in which standard coordinate systems are employed. Introducing a local coordinate system provides the ability to simulate curved metasurfaces with arbitrary shapes. To show the capabilities of the proposed technique, it is applied to different examples including carpet cloaking, illusion and radar echo width (REW) reducing electrically large curved metasurfaces with a size of about 120 times of the wavelength. The proposed method is capable of analyzing both periodic and non-periodic (aperiodic) metasurfaces and works for both transverse electric and transverse magnetic polarizations of the incident field.

The proposed analytical technique consists of two parts: (1) the GSTCs that relate unknown tangential electric and magnetic fields above and below the metasurface boundary and (2) the integral equations based on the extinction theorem that provide another set of equations in terms of unknowns. The integral equations involve periodic Green's function, given by the Floquet expansion and also the tangential electric and magnetic fields at the boundary, given by the Fourier series with unknown coefficients. Unknowns are found using the GSTCs and the integral equations.

The study is organized as follows. In Section 2, problem geometry is introduced. Section 3 reviews GSTC modelling of the metasurface and introduces some assumptions about the susceptibility parameters. Section 4 introduces the integral equations based on the extinction theorem. It provides fields and the periodic Green's function expansions. Finally, it provides a matrix equation to be solved for the unknowns of the problem which are the Fourier coefficients of the tangential electric and magnetic fields. The proposed method is then validated in Section 5. Section 6 discusses the convergence of the approach. Section 7 provides two applications of the proposed analysis, that is, illusion and REW reduction. Finally, conclusions are given in Section 8.

2 | PROBLEM GEOMETRY

Let us consider an electrically large object on the ground. Here, it is assumed that the structure has no variation in the y-direction ($\partial/\partial y \equiv 0$) and an obliquely incident wave illuminates the structure ($k_i = k_{ix}\hat{x} - k_{iz}\hat{z}$). We also assume $e^{j\omega t}$ time convention. The 2D profile is limited to a finite length of L, and is covered by an electrically thin sheet (metasurface) consisting of sub-wavelength cells [9]. Figure 1 shows a periodic metasurface. The profile has no change in the y-direction

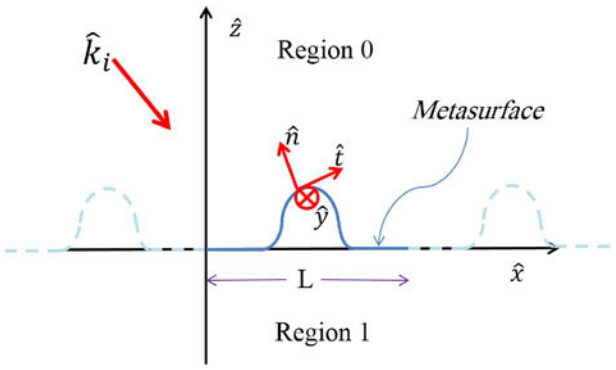

FIGURE 1 An electrically large object on the ground is covered by a metasurface. Regions above and below the metasurface are called regions 0 and 1, respectively. Local coordinates are shown as $\hat{t}$, $\hat{y}$ and $\hat{n}$. L, finite length

and is periodic along the x-direction with periodicity of L. The height profile is assumed to be an arbitrary function of $z = f(x)$. In this analysis, we use the local coordinate system $(\hat{t}, \hat{y}, \hat{n})$ on the metasurface where the normal unit vector is $\hat{n} = (\hat{z} - f'(x)\hat{x})/\sqrt{1 + f'^2(x)}$, $f' = df(x)/dx$, and the tangential unit vector is $\hat{t} = \hat{y} \times \hat{n}$ [34].

3 | GSTCs MODELLING OF THE METASURFACE

Thanks to the GSTCs, the thickness of cells can be ignored and just macroscopic features of the surface are considered. We consider metasurfaces with transversal polarizabilities. In this case, the GSTCs can be written as [25]:

$$\hat{n} \times (\bar{H}_0 - \bar{H}_1) = j\omega(P_t\hat{t} + P_y\hat{y}), \tag{1a}$$

$$(\bar{E}_0 - \bar{E}_1) \times \hat{n} = j\omega\mu_0(M_t\hat{t} + M_y\hat{y}), \tag{1b}$$

where according to Figure 1, $\bar{E}_0(\bar{H}_0)$ and $\bar{E}_1(\bar{H}_1)$ are total electric (magnetic) fields in region 0 and 1, respectively. Also, $P_t(M_t)$ and $P_y(M_y)$ are electric (magnetic) polarizabilities along $\hat{t}$ and $\hat{y}$ directions, given by

$$\begin{bmatrix} P_t \\ P_y \end{bmatrix} = \varepsilon_0 \bar{\bar{\chi}}_{ee} \begin{bmatrix} E_t^{av} \\ E_y^{av} \end{bmatrix} + \frac{\bar{\bar{\chi}}_{em}}{c_0} \begin{bmatrix} H_t^{av} \\ H_y^{av} \end{bmatrix}, \tag{2a}$$

$$\begin{bmatrix} M_t \\ M_y \end{bmatrix} = \frac{\bar{\bar{\chi}}_{me}}{\eta_0} \begin{bmatrix} E_t^{av} \\ E_y^{av} \end{bmatrix} + \bar{\bar{\chi}}_{mm} \begin{bmatrix} H_t^{av} \\ H_y^{av} \end{bmatrix}. \tag{2b}$$

where averaged fields E^{av} and H^{av} are given by $\Psi^{av} = \frac{1}{2}(\Psi_0 + \Psi_1)$ where $\Psi = E$, H and Ψ_0 and Ψ_1 are the fields in regions 0 and 1, respectively. Here, ε_0 is the permittivity, c_0 is the speed of light and η_0 is the wave impedance all in the free-space medium. Furthermore, we assume a non-

gyrotropic metasurface with no cross-polarization scattering. Specifically, non-gyrotropic metasurface requires $\chi_{ee}^{ty}=\chi_{ee}^{yt}=0$, $\chi_{mm}^{ty}=\chi_{mm}^{yt}=0, \chi_{em}^{tt}=\chi_{em}^{yy}=0$ and $\chi_{me}^{tt}=\chi_{me}^{yy}=0$ [35]. Thus, susceptibilities are given by the following relations:

$$\bar{\bar{\chi}}_{ee}=\begin{bmatrix}\chi_{ee}^{tt} & 0\\ 0 & \chi_{ee}^{yy}\end{bmatrix}, \bar{\bar{\chi}}_{mm}=\begin{bmatrix}\chi_{mm}^{tt} & 0\\ 0 & \chi_{mm}^{yy}\end{bmatrix}, \tag{3a}$$

$$\bar{\bar{\chi}}_{em}=\begin{bmatrix}0 & \chi_{em}^{ty}\\ \chi_{em}^{yt} & 0\end{bmatrix}, \bar{\bar{\chi}}_{me}=\begin{bmatrix}0 & \chi_{me}^{ty}\\ \chi_{me}^{yt} & 0\end{bmatrix}. \tag{3b}$$

where matrices in Equation (3a) are diagonal and those in Equation (3b) are off-diagonal.

4 | FORMULATION

According to the extinction theorem [36–38], for $z > f(x)$ we have:

$$\begin{pmatrix}E_{0y}(\bar{\rho})-E_{iy}(\bar{\rho})\\ H_{0y}(\bar{\rho})-H_{iy}(\bar{\rho})\end{pmatrix}=\int_{x_0}^{x_L}\frac{\partial g_{0p}}{\partial n'}\begin{pmatrix}E_{0y}(\bar{\rho}')\\ H_{0y}(\bar{\rho}')\end{pmatrix} - g_{0p}\frac{\partial}{\partial n'}\begin{pmatrix}E_{0y}(\bar{\rho}')\\ H_{0y}(\bar{\rho}')\end{pmatrix}\mathrm{d}l', \tag{4a}$$

$$\begin{pmatrix}0\\ 0\end{pmatrix}=\int_{x_0}^{x_L}\frac{\partial g_{1p}}{\partial n'}\begin{pmatrix}E_{1y}(\bar{\rho}')\\ H_{1y}(\bar{\rho}')\end{pmatrix}-g_{1p}\frac{\partial}{\partial n'}\begin{pmatrix}E_{1y}(\bar{\rho}')\\ H_{1y}(\bar{\rho}')\end{pmatrix}\mathrm{d}l', \tag{4b}$$

and for $z < f(x)$ we have:

$$\begin{pmatrix}E_{1y}(\bar{\rho})\\ H_{1y}(\bar{\rho})\end{pmatrix}=-\int_{x_0}^{x_L}\frac{\partial g_{1p}}{\partial n'}\begin{pmatrix}E_{1y}(\bar{\rho}')\\ H_{1y}(\bar{\rho}')\end{pmatrix} - g_{1p}\frac{\partial}{\partial n'}\begin{pmatrix}E_{1y}(\bar{\rho}')\\ H_{1y}(\bar{\rho}')\end{pmatrix}\mathrm{d}l', \tag{5a}$$

$$\begin{pmatrix}E_{iy}(\bar{\rho})\\ H_{iy}(\bar{\rho})\end{pmatrix}=-\int_{x_0}^{x_L}\frac{\partial g_{0p}}{\partial n'}\begin{pmatrix}E_{0y}(\bar{\rho}')\\ H_{0y}(\bar{\rho}')\end{pmatrix} - g_{0p}\frac{\partial}{\partial n'}\begin{pmatrix}E_{0y}(\bar{\rho}')\\ H_{0y}(\bar{\rho}')\end{pmatrix}\mathrm{d}l', \tag{5b}$$

where $E_{iy}(H_{iy})$ is the incident electric (magnetic) field in region 0. The $\bar{\rho}'=x'\hat{x}+z'\hat{z}$ specifies a point on the surface and $\bar{\rho}=x\hat{x}+z\hat{z}$ shows an observation point. The point x_0 is an arbitrary start point, $x_L = x_0 + L$ is the corresponding end point and $dl'=dx'\sqrt{1+f'^2(x')}$ is the differential length. The Floquet theorem gives us the periodic Green's functions g_{rp} in region above ($r = 0$) and below ($r = 1$) the metasurface given by [36–39].

$$g_{rp}(\bar{\rho},\bar{\rho}')=\frac{-\mathrm{j}}{2L}\sum_{n=-N}^{N}\frac{1}{k_{rnz}}e^{-\mathrm{j}k_{nx}(x-x')-\mathrm{j}k_{rnz}|z-z'|}, \tag{6}$$

where $k_{nx} = k_{ix} + 2n\pi/L$, $k_{rnz}=\sqrt{k_r^2-k_{nx}^2}$, k_r is the wave number in region r and $2N+1$ is the number of Floquet modes. Since we are using the periodic Green's function, we observe that the integrals in Equations (4) and (5) run over the finite interval L and not over an infinite interval. We note that an original 2D periodic Green's function composed of Hankel functions is in fact a slowly converging series [36]. An integral transformation leads to a faster converging series, given by Equation (6) (see page 501 of [36]). We also note that the number of Floquet modes should be sufficiently large in order to have both propagating and evanescent modes to obtain correct results. Here, we set the number of evanescent modes the same as the number of propagating modes [41]. Finally, we remark that in order to analyse the scattering due to the horizontal h and vertical v polarizations of the incident field, we use only the y-component of electric and magnetic fields, respectively.

We note that E_{0y}, H_{0y}, $\partial E_{0y}/\partial n$, $\partial H_{0y}/\partial n$, E_{1y}, H_{1y}, $\partial E_{1y}/\partial n$, $\partial H_{1y}/\partial n$ in Equations (4) and (5) are all unknowns. We first use four scalar equations given by Equations (4b) and (5b) and four scalar equations of the GSTCs given by Equations (1) and (2) to find the eight unknowns. Next, having determined the unknowns, the fields above and below the metasurface are computed using Equations (4a) and (5a). Inserting Equation (6) in Equations (4a) and (4b), we respectively have:

$$\begin{bmatrix}E_{0y}-E_{iy}\\ H_{0y}-H_{iy}\end{bmatrix}=\sum_{n=-N}^{N}\begin{bmatrix}b_n\\ d_n\end{bmatrix}e^{-\mathrm{j}(k_{nx}x+k_{0nz}z)}, \tag{7a}$$

where

$$\begin{bmatrix}b_n\\ d_n\end{bmatrix}=\frac{\mathrm{j}}{2Lk_{0nz}}\int_{x_0}^{x_0+L}\left(\sqrt{1+f'^2(x')}\ \frac{\partial}{\partial n}\begin{bmatrix}E_{0y}\\ H_{0y}\end{bmatrix} + \mathrm{j}(k_{nx}f'(x')-k_{0nz})\begin{bmatrix}E_{0y}\\ H_{0y}\end{bmatrix}\right)e^{\mathrm{j}(k_{nx}x'+k_{0nz}f(x'))}\,\mathrm{d}x' \tag{7b}$$

and

$$\begin{bmatrix}0\\ 0\end{bmatrix}=\sum_{n=-N}^{N}\begin{bmatrix}B_n\\ D_n\end{bmatrix}e^{-\mathrm{j}(k_{nx}x+k_{1nz}z)}, \tag{8a}$$

where

$$\begin{bmatrix} B_n \\ D_n \end{bmatrix} = \frac{-\mathrm{j}}{2Lk_{1nz}} \int_{x_0}^{x_0+L} \left(\sqrt{1+f'^2(x')} \ \frac{\partial}{\partial n} \begin{bmatrix} E_{1y} \\ H_{1y} \end{bmatrix} + \mathrm{j}(k_{nx}f'(x') - k_{1nz}) \begin{bmatrix} E_{1y} \\ H_{1y} \end{bmatrix} \right) e^{\mathrm{j}(k_{nx}x' + k_{1nz}f(x'))} \, \mathrm{d}x'. \tag{8b}$$

Similarly, inserting Equation (6) in Equations (5a) and (5b), we respectively have:

$$\begin{bmatrix} E_{1y} \\ H_{1y} \end{bmatrix} = \sum_{n=-N}^{N} \begin{bmatrix} A_n \\ C_n \end{bmatrix} e^{-\mathrm{j}(k_{nx}x - k_{1nz}z)}, \tag{9a}$$

where

$$\begin{bmatrix} A_n \\ C_n \end{bmatrix} = \frac{-\mathrm{j}}{2Lk_{1nz}} \int_{x_0}^{x_0+L} \left(\sqrt{1+f'^2(x')} \ \frac{\partial}{\partial n} \begin{bmatrix} E_{1y} \\ H_{1y} \end{bmatrix} + \mathrm{j}(k_{nx}f'(x') + k_{1nz}) \begin{bmatrix} E_{1y} \\ H_{1y} \end{bmatrix} \right) e^{\mathrm{j}(k_{nx}x' - k_{1nz}f(x'))} \, \mathrm{d}x' \tag{9b}$$

and

$$-\begin{bmatrix} E_{iy} \\ H_{iy} \end{bmatrix} = \sum_{n=-N}^{N} \begin{bmatrix} a_n \\ c_n \end{bmatrix} e^{-\mathrm{j}(k_{nx}x - k_{0nz}z)}, \tag{10a}$$

where

$$\begin{bmatrix} a_n \\ c_n \end{bmatrix} = \frac{\mathrm{j}}{2Lk_{0nz}} \int_{x_0}^{x_0+L} \left(\sqrt{1+f'^2(x')} \ \frac{\partial}{\partial n} \begin{bmatrix} E_{0y} \\ H_{0y} \end{bmatrix} + \mathrm{j}(k_{nx}f'(x') + k_{0nz}) \begin{bmatrix} E_{0y} \\ H_{0y} \end{bmatrix} \right) e^{\mathrm{j}(k_{nx}x' - k_{0nz}f(x'))} \, \mathrm{d}x'. \tag{10b}$$

Equations (7a), (8a), (9a), and (10a) are the Floquet expansions of the y-component of the fields. The upward and downward going waves in region 0 are respectively given by Equations (7a) and (10a). On the other hand, the upward and downward going waves in region 1 are respectively given by Equations (8a) and (9a). The Floquet coefficients of the upward and downward going waves in each region are shown in Figure 2. As shown in this figure, downward electric and magnetic fields coefficients in region 0, a_n and c_n, are the Floquet expansions of the incident wave (E_{iy}, H_{iy}) as given by Equation (10a). Also, upward electric and magnetic fields in region 1 are equal to zero since there is no source under the metasurface. This is given by Equation (8a).

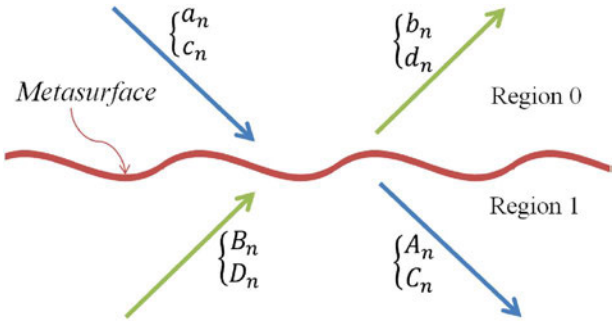

FIGURE 2 Floquet coefficients of the y-component of the downward and upward going electric and magnetic waves are shown. Downward going electric and magnetic fields in region 0 are respectively given by coefficients (a_n, c_n) and those in region 1 are given by (A_n, C_n). Upward going electric and magnetic fields in region 0 are given by (b_n, d_n) and those in region 1 are given by (B_n, D_n)

The left-hand side of Equations (8b) and (10b) are known. We use Equations (8b) and (10b) along with the GSTCs to find the unknowns E_{0y}, H_{0y}, $\partial E_{0y}/\partial n$, $\partial H_{0y}/\partial n$, E_{1y}, H_{1y}, $\partial E_{1y}/\partial n$, $\partial H_{1y}/\partial n$, first. Next, we use Equations (7b) and (9b) to compute amplitude and phase of scattered Floquet modes (b_n, d_n) and (A_n, C_n). Finally, the scattered fields in regions 0 and 1 are calculated using Equations (7a) and (9a), respectively. In this regard, the y-components of the electric and magnetic fields on both sides of the metasurface are expanded by the Fourier series with unknown coefficients. On the surface $z' = f(x')$, Fourier expansions of the y-component of the fields are given by:

$$\begin{bmatrix} E_{1y}(\bar{\rho}') \\ H_{1y}(\bar{\rho}') \end{bmatrix} = \sum_{m=-M}^{M} \begin{bmatrix} \alpha_m \\ \gamma_m \end{bmatrix} e^{-\mathrm{j}k_{mx}x'}, \tag{11a}$$

$$\begin{bmatrix} E_{0y}(\bar{\rho}') \\ H_{0y}(\bar{\rho}') \end{bmatrix} = \sum_{m=-M}^{M} \begin{bmatrix} \tau_m \\ \kappa_m \end{bmatrix} e^{-\mathrm{j}k_{mx}x'}, \tag{11b}$$

where coefficients α_m, γ_m, τ_m and κ_m are unknowns and M is the truncation number for the Fourier expansions. To solve Equations (8b) and (10b), the Green's functions and their normal derivatives can be derived using Equation (6). Also, the y-components of fields in both regions (E_{0y}, H_{0y}, E_{1y}, H_{1y}) are given by their Fourier representations, given by Equation (11). The only terms which must be modified are the normal derivatives of fields ($\partial E_{0y}/\partial n$, $\partial H_{0y}/\partial n$, $\partial E_{1y}/\partial n$, and $\partial H_{1y}/\partial n$). To this end, we first use the Maxwell equations to relate the normal derivative of the fields to the tangential t-components of the fields (H_{rt}, E_{rt}) in each region. After that, the t-components of the fields are rewritten versus the y-components of the fields according to GSTCs.

Using Maxwell equations, we have:

$$E_{rt} = \frac{j\omega\mu_r}{k_r^2}\frac{\partial}{\partial n}H_{ry}, \tag{12a}$$

$$H_{rt} = \frac{-j\omega\varepsilon_r}{k_r^2}\frac{\partial}{\partial n}E_{ry}, \tag{12b}$$

where $r = 0, 1$ is the region number. Next, we use GSTCs, Equations (1a)–(2b), to relate the y-components of the fields to the t-components of them as:

$$\begin{bmatrix} 1-\frac{jk_0}{2}\chi_{em}^{yt} & -1-\frac{jk_0}{2}\chi_{em}^{yt} \\ \frac{j\omega\mu}{2}\chi_{mm}^{tt} & \frac{j\omega\mu}{2}\chi_{mm}^{tt} \end{bmatrix}\begin{bmatrix} H_{0t} \\ H_{1t} \end{bmatrix} = \begin{bmatrix} \frac{j\omega\varepsilon}{2}\chi_{ee}^{yy} & \frac{j\omega\varepsilon}{2}\chi_{ee}^{yy} \\ 1-\frac{jk_0}{2}\chi_{me}^{ty} & -1-\frac{jk_0}{2}\chi_{me}^{ty} \end{bmatrix}\begin{bmatrix} E_{0y} \\ E_{1y} \end{bmatrix}, \tag{13a}$$

$$\begin{bmatrix} -\frac{j\omega\varepsilon}{2}\chi_{ee}^{tt} & -\frac{j\omega\varepsilon}{2}\chi_{ee}^{tt} \\ 1+\frac{jk_0}{2}\chi_{me}^{yt} & -1+\frac{jk_0}{2}\chi_{me}^{yt} \end{bmatrix}\begin{bmatrix} E_{0t} \\ E_{1t} \end{bmatrix} = \begin{bmatrix} 1+\frac{jk_0}{2}\chi_{em}^{ty} & -1+\frac{jk_0}{2}\chi_{em}^{ty} \\ -\frac{j\omega\mu}{2}\chi_{mm}^{yy} & -\frac{j\omega\mu}{2}\chi_{mm}^{yy} \end{bmatrix}\begin{bmatrix} H_{0y} \\ H_{1y} \end{bmatrix}. \tag{13b}$$

Consequently, the tangential fields (E_{rt}, H_{rt}) in terms of the y-components of the fields (E_{ry}, H_{ry}) in both regions $(r = 0, 1)$ are given as:

$$E_{rt} = \frac{H_{1y}-H_{0y}}{j\omega\varepsilon\chi_{ee}^{tt}}\left(1-(-1)^r\frac{jk_0}{2}\chi_{me}^{yt}\right) - \frac{H_{1y}+H_{0y}}{j\omega\varepsilon\chi_{ee}^{tt}}\left(\frac{jk_0}{2}\chi_{em}^{ty}+(-1)^r\frac{k_0^2}{4}(\chi_{em}^{ty}\chi_{me}^{yt}-\chi_{ee}^{tt}\chi_{mm}^{yy})\right), \tag{14a}$$

$$H_{rt} = \frac{E_{0y}-E_{1y}}{j\omega\mu\chi_{mm}^{tt}}\left(1+(-1)^r\frac{jk_0}{2}\chi_{em}^{yt}\right) + \frac{E_{1y}+E_{0y}}{j\omega\mu\chi_{mm}^{tt}}\left((-1)^r\frac{k_0^2}{4}(\chi_{me}^{ty}\chi_{em}^{yt}-\chi_{mm}^{tt}\chi_{ee}^{yy})-\frac{jk_0}{2}\chi_{me}^{ty}\right). \tag{14b}$$

Consequently, using Equations (11), (12) and (14), the normal derivatives of the y-components of the fields are given by the following Fourier series:

$$\frac{\partial}{\partial n}E_{ry} = \sum_m \frac{e^{-jk_{mx}x}}{\chi_{mm}^{tt}}\left[(\tau_m-\alpha_m)\left(1+(-1)^r\frac{jk_0}{2}\chi_{em}^{yt}\right) + (\tau_m+\alpha_m)\left((-1)^r\frac{k_0^2}{4}(\chi_{me}^{ty}\chi_{em}^{yt}-\chi_{mm}^{tt}\chi_{ee}^{yy})-\frac{jk_0}{2}\chi_{me}^{ty}\right)\right], \tag{15a}$$

$$\frac{\partial}{\partial n}H_{ry} = \sum_m \frac{e^{-jk_{mx}x}}{\chi_{ee}^{tt}}\left[(\kappa_m-\gamma_m)\left(1-(-1)^r\frac{jk_0}{2}\chi_{me}^{yt}\right) + \left(\kappa_m+\gamma_m\right)\left(\frac{jk_0}{2}\chi_{em}^{ty}+(-1)^r\frac{k_0^2}{4}(\chi_{me}^{yt}\chi_{em}^{ty}-\chi_{mm}^{yy}\chi_{ee}^{tt})\right)\right]. \tag{15b}$$

Please note that $\chi_{ij}^{pq}, (i, j = e, m), (p, q = t, y)$ may be a constant or a function of x. By substituting Fourier representations Equations (11) and (15) in Equations (8b) and (10b), the following matrix equation is obtained:

$$Q_1\begin{bmatrix} \bar{\alpha} \\ \bar{\tau} \\ \bar{\gamma} \\ \bar{\kappa} \end{bmatrix} = \begin{bmatrix} \bar{a} \\ \bar{c} \\ \bar{B} \\ \bar{D} \end{bmatrix}. \tag{16}$$

where Q_1 is a $(8N + 4) \times (8M + 4)$ matrix (see Appendix A). The Fourier coefficients vectors are defined as $\bar{\zeta} = [\zeta_1, \zeta_2, \ldots\zeta_{2M+1}]^T$, $(\zeta = \alpha, \tau, \gamma, \kappa)$ where $[.]^T$ denotes the transpose of the matrix. Equation (8a) results in zero upward coefficients in region 1 $(\bar{B} = \bar{D} = [\bar{0}]_{(2N+1)\times 1})$ and according to Equation (10a), downward Floquet coefficients $\bar{a}$ and $\bar{c}$ are expansion of $-E_{iy}$ and $-H_{iy}$, respectively. Equation (16) is uniquely solved if the number of considered Floquet modes equals the number of Fourier terms $(N = M)$.

From Equation (16), the Fourier coefficients (α_m, γ_m, τ_m and κ_m) are determined. After that, Equation (15) and the Fourier expansions Equation (11) are substituted into Equations (7b) and (9b) to find Floquet coefficients of scattered fields (b_n, d_n, A_n and C_n). Again, this could be represented by a matrix equation given by:

$$Q_2\begin{bmatrix} \bar{\alpha} \\ \bar{\tau} \\ \bar{\gamma} \\ \bar{\kappa} \end{bmatrix} = \begin{bmatrix} \bar{b} \\ \bar{d} \\ \bar{A} \\ \bar{C} \end{bmatrix}, \tag{17}$$

where Q_2 is a $(8N + 4) \times (8M + 4)$ matrix (see Appendix A). Finally, using Equations (16) and (17), the reflected (b_n, d_n) and transmitted (A_n, C_n) expansion coefficients are given by:

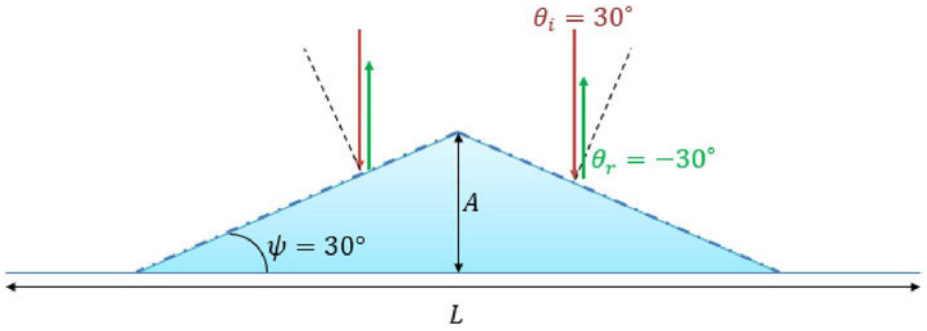

FIGURE 3 A 2D triangular bump with the height of $A = \lambda = 40$ mm and side angles of $\psi = 30°$ is considered to be cloaked at normal incidence

$$\begin{bmatrix} \bar{b} \\ \bar{d} \\ \bar{A} \\ \bar{C} \end{bmatrix} = Q_2 Q_1^{-1} \begin{bmatrix} \bar{a} \\ \bar{c} \\ \bar{B} \\ \bar{D} \end{bmatrix}. \tag{18}$$

Having the expansion coefficients, the reflected and transmitted fields are then calculated using Equations (7a) and (9a), respectively.

To analyse the scattering from a single isolated structure, we need to sufficiently increase the periodicity, L, of the associated periodic structure and show that the solution converges to that of a non-periodic one [40, 41].

5 | VALIDATION

In this section, we verify the method by analysing a cloak structure when illuminated both normally and obliquely. To simulate such aperiodic structures by the Floquet–Fourier (FF) method, we sufficiently increase the periodicity L.

5.1 | Example 1: Cloaking a triangular bump, illuminated normally

Let us consider scattering from a bump put on the perfect electric conductor (PEC) ground. The sides of the bump are covered by the designed metasurfaces. Cells are designed in such a way that when the bump is illuminated by a normally incident plane wave, the field is reflected normally as it is reflected from a flat ground plane. Therefore, the bump would be invisible to the incident wave. Figure 3 shows the studied structure. Here, we consider a relatively small triangular bump with the height of $A = \lambda = 40$ mm, side angles of $\psi = 30°$ and $L \approx 15A$ to be able to simulate the entire problem in the analysis system high frequency structural simulation (ANSYS HFSS) Our current available computer (Intel Core i7-4790K CPU with 4 GHz CPU Clock and 16 GB RAM) restricted us to simulate larger problems. Also, the incident wave has been assumed to have a TE_z (i.e. electric field along the y-axis) polarization.

The unit cell of the metasurface used in this design is shown in Figure 4. As shown, the unit cell is a square loop with the length of a and the width of $w = 0.25$ mm printed on a Rogers 4003 substrate with the thickness of $t = 0.813$ mm. Figure 4 shows the simulated unit cell of the metasurface and its boundary conditions in ANSYS HFSS. As shown in this figure, periodic boundary conditions (PBCs) are used around the cell, and the cell is excited by a plane wave illuminated obliquely at the $\theta_i = \pm 30°$ with respect to the z-axis. It should be noted that since the cells lie on a bump with the slope of $\psi = 30°$ (see Figure 3), a plane wave normally incident on the bump makes an angle of $\theta_i = 30°$ with respect to the normal to the cell surface. That is why in the unit cell simulation (see Figure 4), the angle of incidence is considered as 30°. Using the mentioned setup, the reflection scattering parameter, S_{11}, is computed by the ANSYS HFSS and the results are shown in Table 1 for cells used in the cloak. According to the table, the length of the loop a is tuned to provide proper reflection phase and amplitude, at the operation frequency of 7.5 GHz.

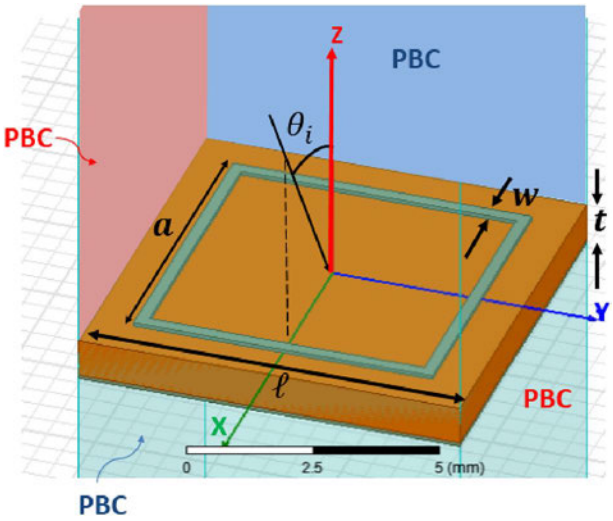

FIGURE 4 The unit cell structure and the simulation setup. The dimension of each cell is $\ell = 8$ mm and the thickness of conductors is 80 μm. Periodic boundary conditions (PBCs) and an oblique incident field along $\theta_i = 30°$ is assumed

Having the scattering parameters calculated by ANSYS HFSS, using Equations (1a) and (1b) the susceptibilities can be calculated as [42]:

$$\chi_{ee}^{tt} = \frac{2\eta_0(H_{0y} - H_{1y})}{-jk_0(E_{0t} + E_{1t})},\ \chi_{mm}^{yy} = \frac{-2(E_{0t} - E_{1t})}{jk_0\eta_0(H_{0y} + H_{1y})}, \tag{19a}$$

$$\chi_{ee}^{yy}=\frac{2\eta_0(H_{0t}-H_{1t})}{jk_0(E_{0y}+E_{1y})},\ \chi_{mm}^{tt}=\frac{2(E_{0y}-E_{1y})}{jk_0\eta_0(H_{0t}+H_{1t})}, \quad (19b)$$

where we assumed that $\bar{\bar{\chi}}_{me}$ and $\bar{\bar{\chi}}_{em}$ are negligible. Since unit cells are symmetric, $\chi_{ee}^{tt}=\chi_{ee}^{yy}$ and $\chi_{mm}^{tt}=\chi_{mm}^{yy}$. Using this symmetry relation, Equation (19) reduces to

$$\chi_{ee}^{tt}=\chi_{ee}^{yy}=\frac{2(1-S_{11})}{jk_0(1+S_{11})\cos\theta_i}, \quad (20a)$$

$$\chi_{mm}^{tt}=\chi_{mm}^{yy}=\frac{2(1+S_{11})\cos\theta_i}{jk_0(1-S_{11})}. \quad (20b)$$

TABLE 1 The size of loop *a* in each unit cell, the associated S-parameters and surface susceptibilities

a(mm)	$\lvert S_{11}\rvert$	$\angle S_{11}$	$\chi_{ee}^{tt}\times 10^3$	$\chi_{mm}^{yy}\times 10^3$
6.685	0.9359	−130.76°	31.9-j2.8	−5.0-j0.4
6.596	0.7992	−58.19°	8.0-j2.1	−18.8-j5.0
6.558	0.7735	+13.24°	−1.6-j1.9	42.2-j47.9
6.485	0.8905	+86.56°	−13.7-j1.6	11.6-j1.3
5.6	0.9985	+158.55°	−77.6-j0.3	2.0

$j=\sqrt{(-1)}$

Computed susceptibilities are listed in Table 1, for each unit cell used in the designed cloak. Then these calculated susceptibilities Equation (20) are used in the FF method to simulate scattering from the bump. In this calculation, we use Huygen's principle to calculate the far-field scattered fields using the near-field total electric and magnetic field values. We assume an imaginary surface *C* near and around the structure and calculate the total fields over that by Equations (7a) and (9a). Then, the equivalent electric and magnetic currents on *C* are given by $\vec{J}(\bar{r}')=\hat{n}\times\vec{H}(\bar{r}')$ and $\vec{M}(\bar{r}')=\vec{E}(\bar{r}')\times\hat{n}$ where $\vec{H}$ and $\vec{E}$ are the total magnetic and electric fields on the curve *C* and $\hat{n}$ is the normal unit vector to the curve *C*. The far-field scattered electric field $E_y^{ff}(\bar{r})$ is then given by:

$$E_y^{ff}(\bar{r})=jk_0\int_C\left(M_t(\bar{r}')\hat{r}\cdot\hat{n}-\eta_0 J_y(\bar{r}')\right)g(\bar{r},\bar{r}')d\bar{r}' \quad (21)$$

where the 2D free-space Green's function $g(\bar{r},\bar{r}')=\frac{-j}{4}H_0^{(2)}(k_0R)$, $R=|\bar{r}-\bar{r}'|$ is used in which $H_0^{(2)}(.)$ is the zeroth-order Hankel function of the second kind and $\hat{r}$ denotes the observation direction.

Figure 5 (b) compares the scattered field computed by the FF technique and the ANSYS HFSS where a very good agreement is observed almost everywhere within the interval $-50°<\theta<+50°$. Only at angles very far from the

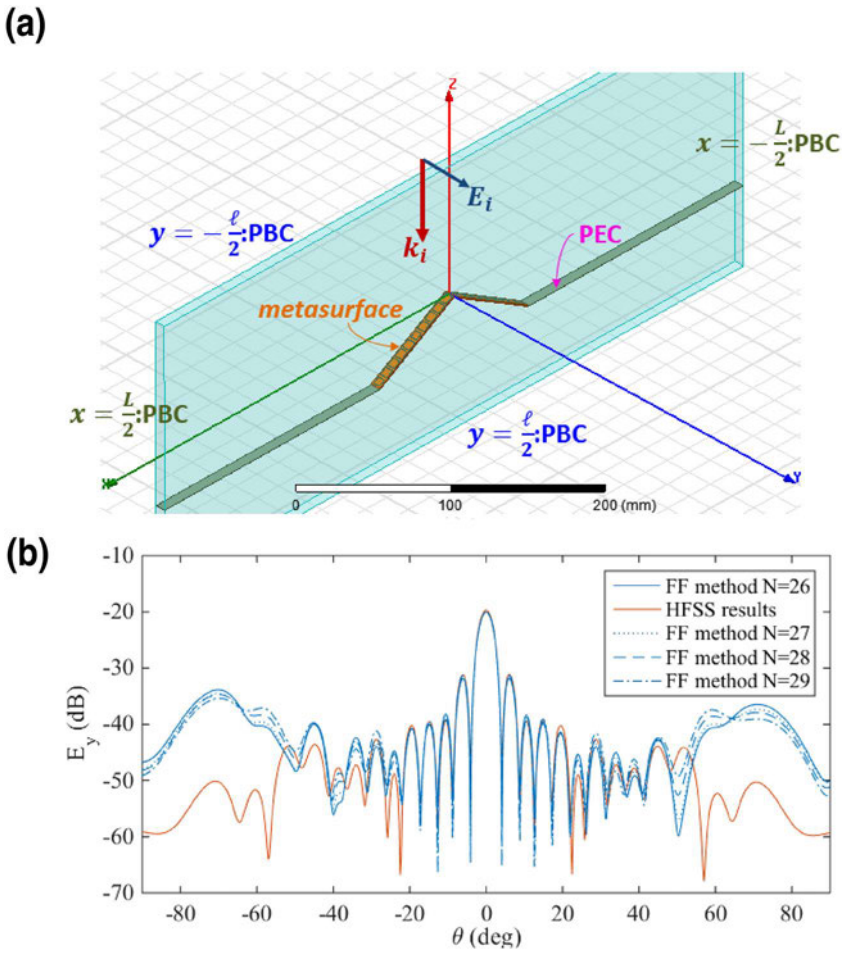

FIGURE 5 (a) Simulated structure in the ANSYS HFSS. (b) Scattering from the bump computed by the ANSYS HFSS and the Floquet-Fourier (FF) method with different number of modes ($2N+1$). PBC, periodic boundary condition; PEC, perfect electric conductor

main beam, there is a distinguishable difference between the HFSS results and the FF results due to the limited number of cells. Ideally, if the bump size and consequently the number of cells increases, then we expect that the difference between the simulation results in the ANSYS HFSS and the FF vanishes.

According to Figure 5 (a), we put the 2D bump inside a vacuum box in order to simulate the structure in ANSYS HFSS. The length and width of the vacuum box are respectively L (periodicity of the structure) and ℓ (dimension of the cell). The height of the box is sufficiently large (e.g. 5λ). The boundary conditions on the box sides, perpendicular to the y and the x axes are PBCs and those on top and bottom of the box, perpendicular to the z axis are the radiation boundary conditions. The plane wave is normally illuminating the structure.

Figure 5 (b) compares HFSS simulation results with those of the FF method for four different numbers of modes. It shows that the FF solution does not significantly change if the number of modes is about $N = 28$.

5.2 | Example 2: Cloaking a triangular bump, illuminated obliquely

Here, we simulate the carpet cloaking problem in [7] by the FF method. A carpet cloak with a triangular bump shape with side angles of 21° is considered. This problem was investigated experimentally in [7]. The structure is computationally too large to be simulated by the HFSS. As shown in Figure 6, the metasurface was designed such that an obliquely incident wave with $\theta_i = 45°$ is reflected at $\theta_{r1} = 25°$ and $\theta_{r2} = 65°$ from two sides of the bump.

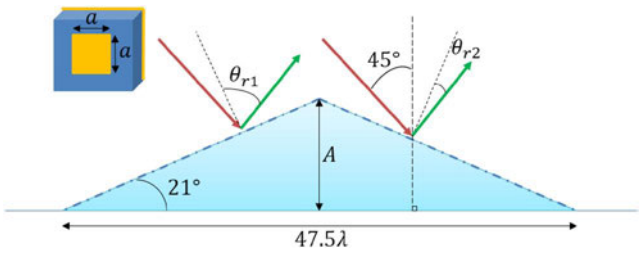

FIGURE 6 Triangular bump with side angles 21°, $A = 9.1\ \lambda$ at the frequency of 0.75 THz, $\theta_i = 45°$, $\theta_{r1} = 25°$, and $\theta_{r2} = 65°$. The unit cell of the metasurface is shown in the top left [7]

Metasurface unit cells, as designed in [7], are square patches on a grounded substrate. The susceptibility parameters are calculated by the relation Equation (20). The metasurface is located only on the bump and the flat surfaces at $z = 0$ are assumed to be perfect conductors. In this simulation, we are assuming the periodicity of $L \approx 205\ \lambda$ and the number of Floquet modes $2N + 1 = 415$. Figure 7 shows the scattered E_y fields using the FF method. As expected, the scattering from the bump is along with $\theta_r = 45°$. The diffraction observed at the sides of Figure 7 are due to the periodic nature of the structure and can be decreased by increasing the periodicity. According to Figure 4 (b) of [43], the scattering of the bump has two dominant components: (1) the specular direction mode which is the stronger one and (2) the mode in the backscattering direction which is the weaker one that (slightly) disturbs the wave fronts, observed in Figure 7.

Figure 8 compares FF simulated scattered fields with measured results reported in Figure 5(p) of [7] with respect to the grazing angle $\psi = 90 - \theta$ degrees. We observe a very good agreement between the two results for almost the entire ψ range, $0 < \psi < 90$ except near (1) the horizon where $\psi < 15$ and (2) normal direction where $\psi > 80$. The discrepancy may be due to a couple of factors, (1) the finite periodicity, set in the FF method, (2) inaccuracy of the synthesized susceptibilities in modelling scattering away from the specular direction.

6 | CONVERGENCE

In this section, we want to show that by increasing the periodicity the scattering converges to that of a single isolated structure which is like a flat PEC ground. Let us assume a Gaussian bump with $f(x) = Ae^{-(x/\alpha)^2}$, and $\alpha = 0.2$ and $A = 4\ \lambda$. By putting a carpet cloak on top of the bump, we want to have a normal reflection from a flat surface due to the normal incident plane wave as if there was no bump.

Therefore, for each cell at $(x, f(x))$ of the metasurface the scattering parameter $S = e^{i\phi}$ is calculated by setting $\phi = \pi - 2k_0 f(x)$. Next, the susceptibilities are computed using Equation (20). For a metasurface with the periodicity of $L \approx 66\ \lambda$, synthesized susceptibilities are shown in Figure 9.

The computed scattered fields are shown in Figure 10. As shown, the reflected field is similar to that of a flat surface, illustrating an excellent performance of the carpet cloak.

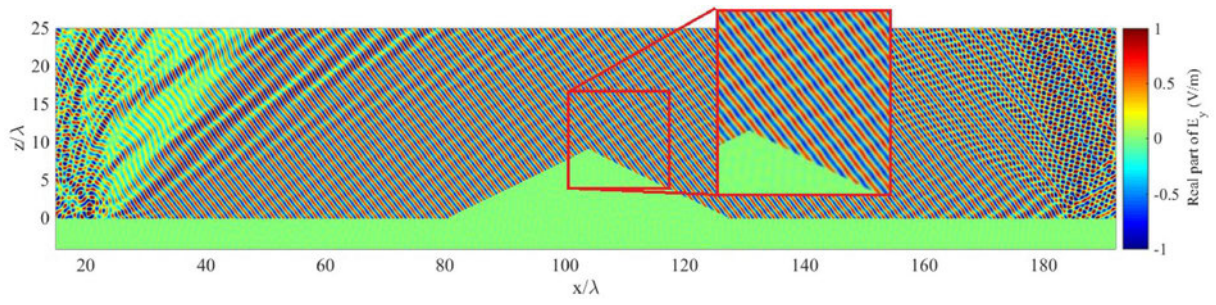

FIGURE 7 Real part of the y-component of the scattered electric field. The parameters are $A = 9.1\ \lambda$, $L \approx 23A$, $f = 750$ GHz and $\theta_i = \theta_r = 45°$

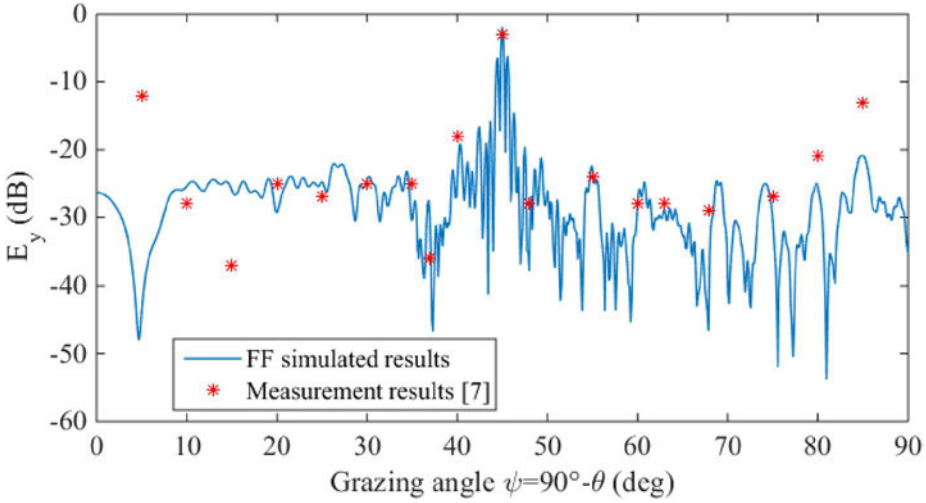

FIGURE 8 Comparison of the FF simulated E_y and the measured results of [7]. FF, Floquet–Fourier

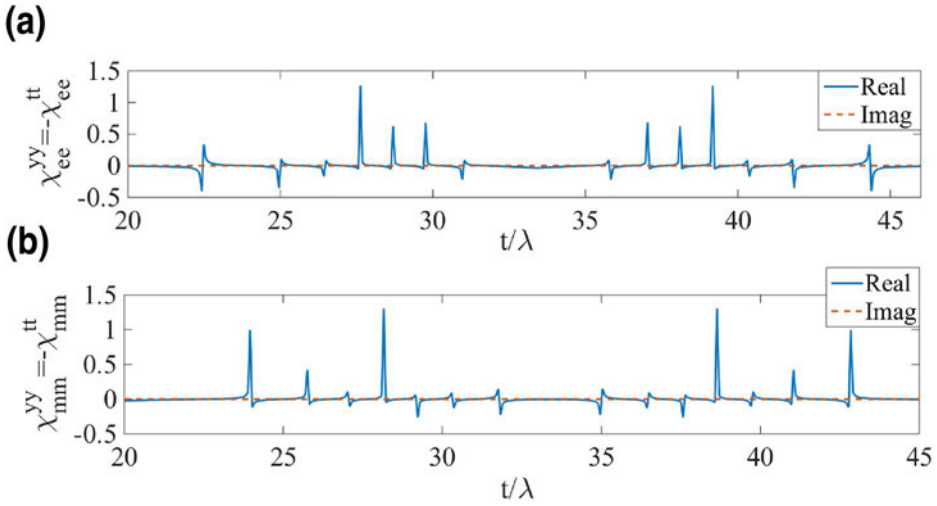

FIGURE 9 Real and imaginary parts of GSTC susceptibility parameters, (a) $\chi_{ee}^{yy} = -\chi_{ee}^{tt}$ and (b) $\chi_{mm}^{yy} = -\chi_{mm}^{tt}$ for the Gaussian bump metasurface with $A = L/18$, $L = 2$ m $\approx 66\ \lambda$ at 10 GHz designed for normal reflection due to normal incidence. Here, in the horizontal axis $t(x)$ is peripheral length along the vector t (see Figure 1), given by $t(x) = \int_0^x \sqrt{1 + f'^2(\xi)}d\xi$. GSTC, generalized sheet transition conditions

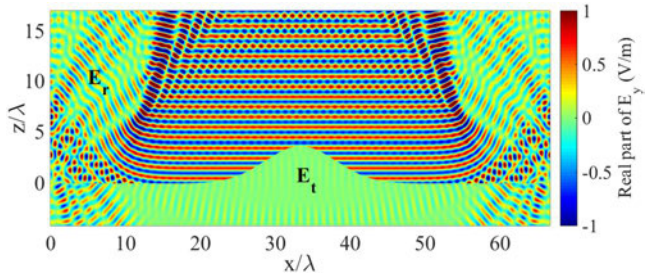

FIGURE 10 Real part of the scattered field y-component. The susceptibility parameters are those shown in Figure 9. Here, L is 2 m $\approx 66\ \lambda$

According to Figure 10, carpet cloak works well in the centre region of the structure up to about 30 λ away from the bump. On the far two sides of the bump, similar to what we have observed in Figure 7, there are diffractions that decrease if the periodicity increases.

Let us show that by running two simulations and assuming two different large periodicities. Figures 11 (a and b) show the results for the periodicity of $L \approx 100\ \lambda$ and $L \approx 133\ \lambda$, respectively. As a result, the width of the centre region, where the reflected wave is almost ideally that of flat ground, enlarges to about 70 λ and 90 λ, respectively. Comparison of Figures 10 and 11 clarifies that as the periodicity increases, diffraction decreases, and the results converge to the scattering from a flat PEC ground plane. Figure 12 compares the reflected power from the coated bump for different periodicities and that of a flat PEC ground. Here, we considered the scattering of the flat PEC ground as a reference which is computed analytically. We observe that the reflected power along the $+z$ axis tends to that of the flat ground as the periodicity L increases.

Table 2 shows the number of Floquet modes $2N + 1$ and the simulation run times for different periodicity values of L. The number of segments for integrations is assumed fixed for

all cases to fairly compare the simulation run times. According to Table 2, as periodicity L increases, the number of modes is increased. The results of Table 2 also show that the proposed method can analyse large structures in a considerably short time. All the simulations mentioned in the table are performed for the case of $\theta_i = \theta_r = 0°, f = 10$ GHz with the assumption of no transmission. In other words, since the back of the meta-cells covered by metallic ground, no field could transmit. Therefore, cells are one-sided, reflecting/absorbing the incident power.

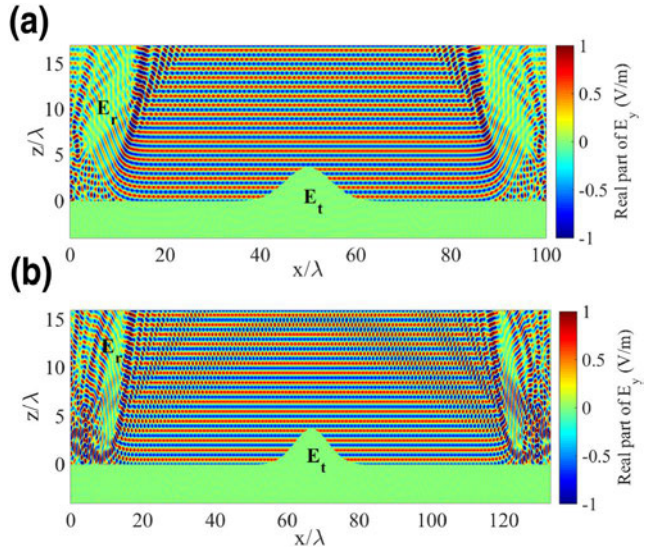

FIGURE 11 Real part of the scattered field y-component. (a) $L = 3$ m $\approx 100\ \lambda$ (b) $L = 4$ m $\approx 133\ \lambda$

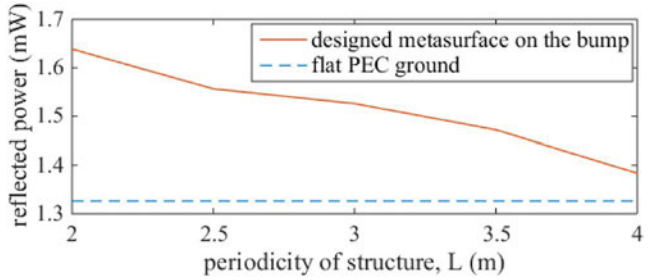

FIGURE 12 As the periodicity L increases, the scattering from two sides vanishes and the reflected power converges to that of a single isolated bump covered by metasurface (which ideally acts as a flat ground)

TABLE 2 Simulation run time versus number of modes for various periodicities, with an Intel Core i7-4790K CPU with 4 GHz CPU clock, and 16 GB RAM

$2N+1$	L(m)	Number of sections in integrations	Time (s)
137	2 m $\approx 66\lambda$	1000	54.603
171	2.5 m $\approx 83\lambda$	1000	74.930
199	3 m $\approx 100\lambda$	1000	96.063
233	3.5 m $\approx 116\lambda$	1000	124.954
271	4 m $\approx 133\lambda$	1000	164.261

7 | APPLICATIONS

In this section, two applications of the FF analysis method: (1) illusion and (2) REW reduction are demonstrated. Here, we note that the GSTCs provide an appropriate model for the design of a multi-mode scattering metasurface rather than the phase gradient model that provides only the zeroth-order mode reflection or transmission.

To synthesize a multi-mode scattering metasurface, the incident and scattered fields in both regions 0 and 1 are first calculated. Then, Equation (19) is used to compute the susceptibilities.

7.1 | Illusion

For the illusion problem, a metasurface is put on an object in such a way that the scattering pattern of the whole structure becomes that of an illusory scatterer. Here, we assume a flat metasurface is put at $z = f(x) = A$ and hides an unknown arbitrary object. We want to pretend that the object is a Gaussian hill on the ground. In the synthesis problem, desired fields (also called pretended fields) are those scattered by the hill $f(x) = Ae^{-(x/\alpha)^2}$ where $\alpha = 0.2$ and $A = L/12 = 5.5\lambda$ while a normal plane wave is illuminating the flat metasurface. It is made of a dielectric with $\varepsilon_{r1} = 4$. The scattering from the pretended Gaussian hill alone, once there is no metasurface is computed and shown in Figure 13(a). This is the desired scattered field.

For calculating the scattering from the pretended dielectric hill, the procedure explained in Section 4 is repeated except that the Fourier expansions of tangential fields in region 1

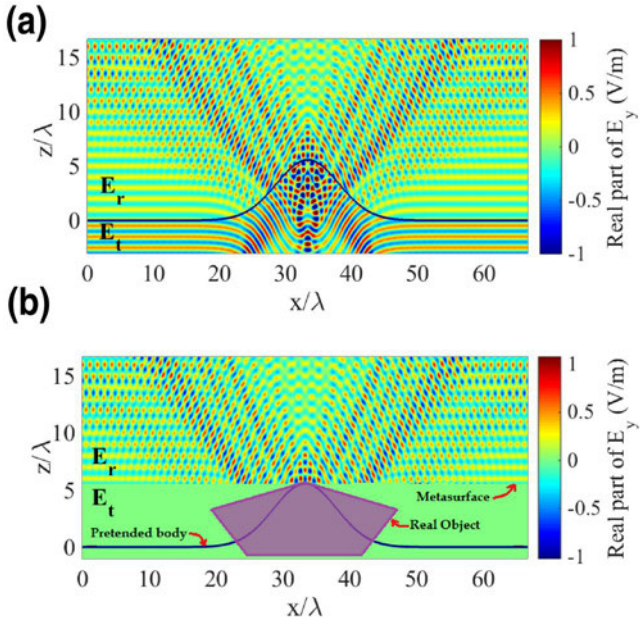

FIGURE 13 (a) Real part of the scattered field from the hill due to a normally incident plane wave at $f = 10$ GHz. The hill has a Gaussian profile with $\alpha = 0.2$ height of $A = L/12$ and the relative permittivity $\varepsilon_{r1} = 4$. The periodicity is $L = 2$ m. (b) Real part of the scattered field from the synthesized metasurface placed at $z = A$

(Equation (11a)) is replaced by the expansion of the normal derivatives of fields in region 0 as follows:

$$\sqrt{1+f'^2(x)}\ \frac{\partial}{\partial n}\begin{bmatrix} E_{0y}(\bar{\rho}) \\ H_{0y}(\bar{\rho}) \end{bmatrix} = \sum_{m=-M}^{M} \begin{bmatrix} \xi_m \\ \nu_m \end{bmatrix} e^{-\mathrm{j}k_{mx}x}. \quad (22)$$

where coefficients τ_m, κ_m, ξ_m, ν_m are unknowns.

Next, considering the normal incident field and the desired ones shown in Figure 13(a), one can synthesize susceptibilities using Equation (19). The synthesized susceptibilities are shown in Figure 14 on the next page. Finally, the scattered fields from the synthesized metasurface are obtained as shown in Figure 13(b). As illustrated, calculated scattered fields in Figure 13(b) are in an excellent agreement with the desired ones in Figure 13(a).

The amplitudes of different scattered modes are plotted in Figure 15(a). The relative errors of the metasurface scattering modes b_n^{m} are given by:

$$\mathrm{RE}(n) = \frac{|b_n^{\mathrm{m}} - b_n^{\mathrm{p}}|}{|b_n^{\mathrm{p}}|} \quad (23)$$

where b_n^{p} is the scattering mode of the pretended hill and n is the Floquet mode number. Figure 15(b) shows the relative error. As shown in this figure, the relative error for all modes is less than 8%.

7.2 | Radar echo width reduction

To reduce mono-static REW, the 2D counterpart of the RCS, is desired to reflect the wave in directions other than the incident one. Here, a metasurface is designed to spread the incident plane wave power in many different directions to reduce the mono-static REW.

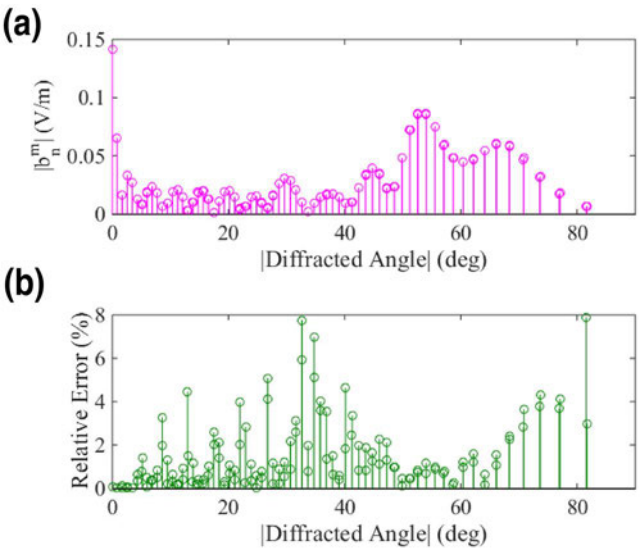

FIGURE 15 (a) Amplitude of the scattered field $E_{0y} - E_{iy}$ modes from the metasurface of Figure 13 in terms of diffraction angles and (b) the relative error computed by Equation (23)

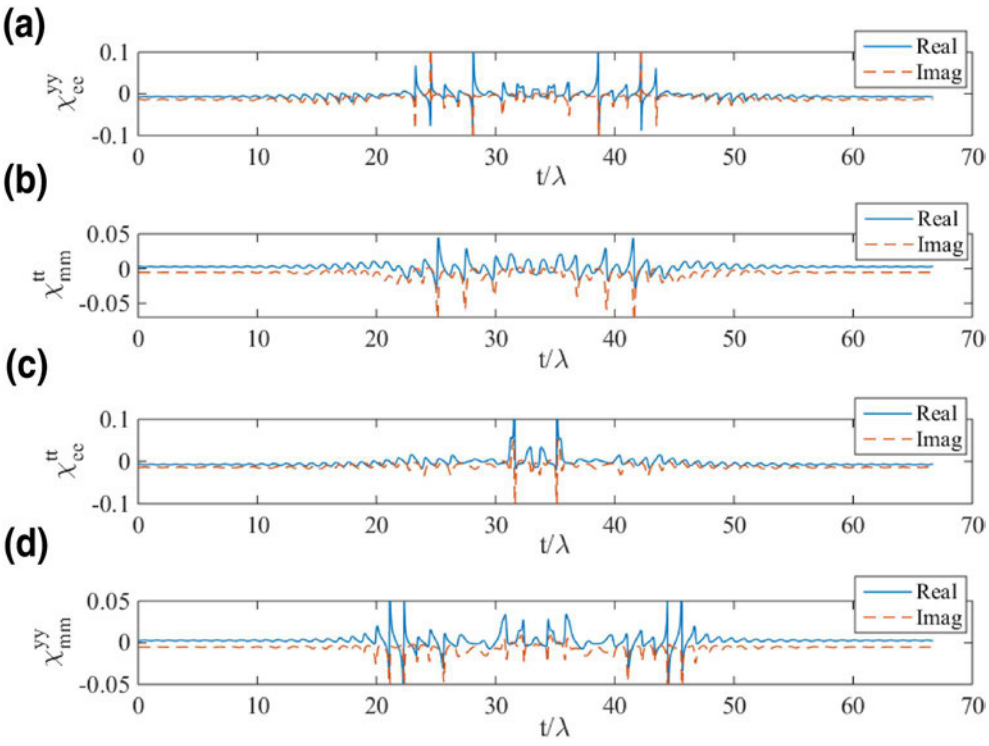

FIGURE 14 The GSTC susceptibilities: (a) χ_{ee}^{yy}, (b) χ_{mm}^{tt}, (c) χ_{ee}^{tt} and (d) χ_{mm}^{yy} synthesized for a normal incident and desired scattered fields of Figure 13. GSTC, generalized sheet transition conditions

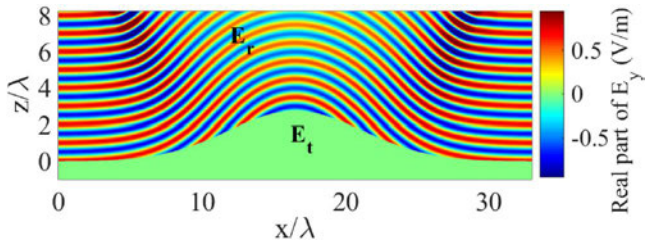

FIGURE 16 Real part of the scattered electric field the y-component. The surface is a periodic Gaussian metallic bump with $L = 1$ m and $A = L/12$. The frequency is $f = 10$ GHz, and incidence angle is $\theta_i = 0°$

First, the scattering of a perfectly conducting bump given by the Gaussian function $f(x) = Ae^{-(x/\alpha)^2}$ where $\alpha = 0.2$ and $A = L/12 \approx 2.77\lambda$ is analysed. To do so, the procedure of Section 7. A is repeated except that the dielectric boundary condition is replaced by the PEC. In the case of PEC, electric and magnetic fields in region one are zero and the tangential electric fields in region 0 are zero ($E_{0y} = E_{0t} = 0$). Thus, tangential derivatives $\partial/\partial t$ of the above fields are also zero resulting in $\partial H_{0y}/\partial n = 0$. Because of the perfect electric boundary condition, $\tau_m = \nu_m = 0$. Using Equations (10a) and (10b), scattered fields are then calculated. Figure 16 shows the scattered electric field from the conducting bump.

The REW is defined as [44].

$$\sigma_{2D} = \lim_{r\to\infty} 2\pi r \left|\frac{E_s}{E_i}\right|^2 = \lim_{r\to\infty} 2\pi r \left|\frac{P_s}{P_i}\right|, \tag{24}$$

where E_s (P_s) and E_i (P_i) are scattered and incident electric fields (power densities), respectively. Since fields are expanded in terms of Floquet coefficients, scattered and incident powers are given by the Floquet coefficients as:

$$\begin{aligned} |P_s| &= \frac{1}{2}|E_{0t}H_{0y}^* - E_{0y}H_{0t}^*| \\ &= \frac{\omega}{2k_0^2}\sum_{n=-N}^{N}\left[\varepsilon_0 k_{0nz}^*|b_n|^2 + \mu_0 k_{0nz}|d_n|^2\right], \end{aligned} \tag{25a}$$

$$|P_i| = \frac{\omega}{2k_0^2}\sum_{n=-N}^{N}\left[\varepsilon_0 k_{0nz}^*|a_n|^2 + \mu_0 k_{0nz}|c_n|^2\right]. \tag{25b}$$

For the metallic bump, monostatic REW is 0.0738 m. Next, a metasurface is synthesized to scatter the normal incident plane wave to six plane waves with equal amplitude in directions of $\theta_1 = 20°$, $\theta_2 = 30°$ and $\theta_3 = 40°$ at planes of $\phi_1 = 0°$ and $\phi_2 = 180°$. Figure 17 shows the synthesized susceptibilities of the metasurface. The desired scattered waves are shown in Figure 18(a). The scattering from the bump with the metasurface is shown in Figure 18(b). As expected, the results of Figure 18(b) are in excellent agreement with those in Figure 18(a).

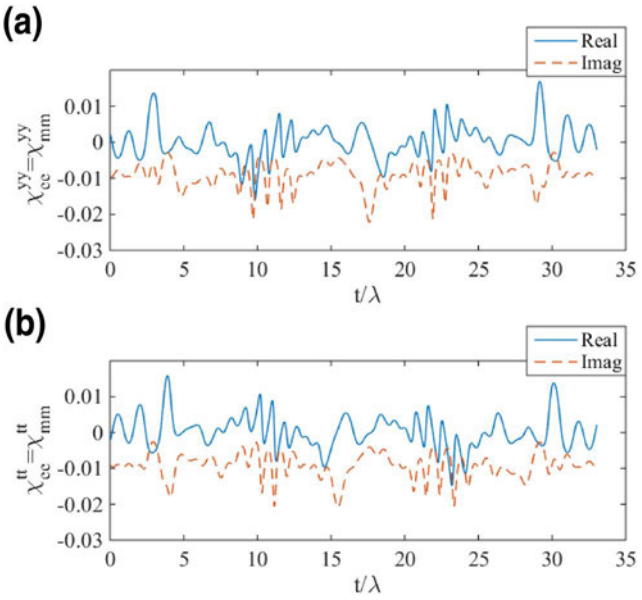

FIGURE 17 Real and imaginary parts of GSTC susceptibility parameters: (a) $\chi_{ee}^{yy} = \chi_{mm}^{yy}$ and (b) $\chi_{ee}^{tt} = \chi_{mm}^{tt}$ calculated for the Gaussian bump with $A = L/12$, $L = 1$ m $\approx 33\lambda$ at 10 GHz for a normal incident plane wave and desired scattered fields shown in Figure 18 (a). GSTC, generalized sheet transition conditions

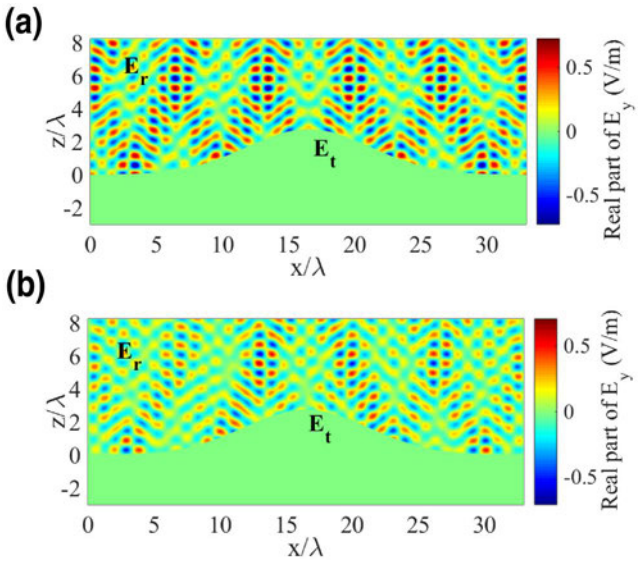

FIGURE 18 (a) Real part of the desired scattered field y-component which is a superposition of six plane waves with propagation directions along $\theta_1 = 20°$, $\theta_2 = 30°$ and $\theta_3 = 40°$ at two planes $\phi_1 = 0°$ and $\phi_2 = 180°$ and (b) Real part of the scattered field from the synthesized metasurface due to the normal incident plane wave. The Gaussian profile is that mentioned in Figure 16

To reduce monostatic REW, power scattered by the bump is spread out in six directions other than the incident one. The

metasurface reduces the REW to 0.0069 m, which is more than 10 times smaller than that of the bump without the metasurface, 0.0738 m.

8 | CONCLUSION

Here, using the Extinction theorem in conjunction with the Floquet and Fourier expansions, a new analytical method is proposed to calculate scattering from 2D electrically large curved metasurfaces. Initially, scattered fields were expanded in terms of the Floquet diffracted modes. Then, by enlarging the periodicity of the structure, couplings between adjacent structures were reduced. Thus, the method was used to analyse non-periodic structures. It also uses susceptibilities to analyse metasurfaces which are dependent on the incident angle for each cell. It was shown that calculated patterns by the proposed method are in good agreement with those of numerical methods (i.e. FEM). The proposed FF method is fast and efficient compared to other numerical approaches performed by commercial software packages. To illustrate its performance, the method was successfully used for different applications such as carpet cloaking, illusion, and mono-static REW reduction. The method has the potential to be generalized for multi-layer metasurfaces analysis.

REFERENCES

1. Engheta, N., Ziolkowski, R.W.: Metamaterials, Physics and Engineering Explorations, 1st edn. John Wiley and Sons Pub. USA (2006)
2. Simovski, C.R.: Material parameters of metamaterials (a review). J. Opt. Spectrosc. 107(5), 726–753 (2009)
3. Oliveri, G., Werner, D.H., Massa, A: Reconfigurable electromagnetics through metamaterials: a review. J. Proc. IEEE. 103(7), 1034–1056 (2015)
4. Yousefi, L., Boybay, M.S., Ramahi, O.M.: Characterization of metamaterials using a strip line fixture. IEEE Trans. Antenn. Propag. 59(4), 1245–1253 (2011)
5. Kabiri, A., et al.: On the fundamental limitations of artificial magnetic materials. IEEE Trans. Antenn. Propag. 58(7), 2345–2353 (2010)
6. Ni, X., et al.: An ultrathin invisibility skin cloak for visible light. J. Sci. 349(6254), 1310–1314 (2015)
7. Wei, M., et al.: Ultrathin metasurface-based carpet cloak for terahertz wave. Opt. Exp. 25(14), 15635–15642 (2017)
8. Wang, R., et al.: Creation of an arbitrary electromagnetic illusion using a planar ultrathin metasurface. J. IEEE Photonics. 9(4), 1–9 (2017)
9. Chen, H.T., et al.: A review of metasurfaces: physics and applications. Rep. Prog. Phys. 79, 076401 (2016)
10. Shameli, M.A., Yousefi, L.: Absorption enhancement in thin-film solar cells using an integrated metasurface lens. J. Opt. Soc. Am. B. 35, 223–230 (2018)
11. Shameli, M.A., et al.: Light trapping in thin film solar cells using a polarization independent phase gradient metasurface. J. Opt. 20(12) 125004 (2018)
12. Salami, P., Yousefi, L.: Far-field subwavelength imaging using phase gradient metasurfaces. J. Lightwave Technol. 37(10), 2317–2323 (2019)
13. Pedross-Engel, A., et al.: Orthogonal coded active illumination for millimeter wave, massive-MIMO computational imaging with metasurface antennas. IEEE Trans. Comput. Imaging. 4(2), 184–193 (2018)
14. Lipworth, G., et al.: Metamaterial apertures for coherent computational imaging on the physical layer. J. Opt. Soc. Am. 30(8), 1603–1612 (2013)
15. Raeker, B.O., Rudolph, S.M.: Arbitrary transformation of antenna radiation using a cylindrical impedance metasurface. IEEE Antenn. Wirel. Propag. Lett. 15, 1101–1104 (2016)
16. Raeker, B.O., Rudolph, S.M.: Verification of arbitrary radiation pattern control using a cylindrical impedance metasurface. IEEE Antenn. Wirel. Propag. Lett. 16, 995–998 (2017)
17. Sipus, Z., et al.: Modelling cascaded cylindrical metasurfaces using sheet impedances and a transmission matrix formulation. IET Microw. Antenn. Propag. 12, 1041–1047 (2018)
18. Chen, P.-Y., Alù, A.: Mantle cloaking using thin patterned metasurfaces. Phys. Rev. B. 84,. 205110 (2011)
19. Padooru, Y.R., et al.: Line-source excitation of realistic conformal metasurface cloaks. J. Appl. Phys. 112, 104902 (2012)
20. Soric, J.C., et al.: Dual-polarized reduction of dipole antenna blockage using mantle cloaks. IEEE Trans. Antenn. Propag. 63, 4827–4834 (2015)
21. Vellucci, S., et al.: Scattering manipulation and camouflage of electrically small objects through metasurfaces. Phys. Rev. Appl. 7, 034032 (2017)
22. Yang, Y., et al.: Full-polarization 3D metasurface cloak with preserved amplitude and phase. J. Adv. Mater. 28(32), 6866–6871 (2016)
23. Yu, N., et al.: Light propagation with phase discontinuities: generalized laws of reflection and refraction. Science. 334, 333–337 (2011)
24. Farmahini-Farahani, M., Mosallaei, H.: Birefringent reflectarray metasurface for beam engineering in infrared. Opt. Lett. 38(4) (2013)
25. Achouri, K., et al.: General metasurface synthesis based on susceptibility tensors. IEEE Trans. Antenn. Propag. 63(7), 2977–2991 (2015)
26. Kuester, E.F., et al.: Averaged transition conditions for electromagnetic fields at a metafilm. IEEE Trans. Antenn. Propag. 51(10) (2003)
27. Sandeep, S., Huang, S.Y.: Simulation of circular cylindrical metasurfaces using GSTC-MoM. J. Multiscale Multiphys. Comput. Tech. 3, 185–192 (2018)
28. Smy, T.J., Gupta, S.: Finite-difference modelling of broadband Huygens metasurfaces based on generalized sheet transition conditions. IEEE Trans. Antenn. Propag. 65(5), 2566–2577 (2017)
29. Hosseini, K., Atlasbaf, Z.: PLRC-FDTD modelling of general GSTC-based dispersive bianisotropic metasurfaces. IEEE Trans. Antennas Propag. 66(1), 262–270 (2018)
30. Vahabzadeh, Y., et al.: Computational analysis of metasurfaces. IEEE J. Multisc. Multiphys. Comput. Techn. 3, 37–49 (2018)
31. Chamanara, N., et al.: Efficient analysis of metasurfaces in terms of spectral-domain GSTC integral equations. IEEE Trans. Antenn. Propag. 65(10), 5340–5347 (2017)
32. Han Teo, J.Y., et al.: Controlling electromagnetic fields at boundaries of arbitrary geometries. J. Phys. Rev. A. 94, 023820 (2016)
33. Jia, X., et al.: Synthesis of Spherical Metasurfaces Based on Susceptibility Tensor GSTCs. arXiv (2017)
34. Foroozesh, A., et al.: Beam focussing using backward-radiating waves on conformal leaky-wave antennas based on a metal strip grating. IEEE Trans. Antenn. Propag. AP-63, 4667–4677 (2015)
35. Dehmollaian, M., et al.: Comparison of Tensor Boundary Conditions (TBCs) with Generalized Sheet Transition Conditions (GSTCs). arXiv (2019)
36. Kong, J.A.: Electromagnetic Wave Theory, 1st edn., pp. 499. John Wiley and Sons Pub. USA (1986)
37. Ishimaru, A.: Electromagnetic Wave Propagation, Radiation, and Scattering From Fundamentals to Applications, 2nd edn., 170. John Wiley and Sons Pub. USA (2017)
38. Peterson, A.F., et al.: Computational Methods for Electromagnetics, 14. IEEE Press New York (1998)
39. Tsang, L. et al.: Scattering of Electromagnetic Waves, Numerical Simulations, 1st edn., pp. 65. John Wiley and Sons Pub. USA (2001)
40. Kuo, C., Moghaddam, M.: Electromagnetic scattering from multilayer rough surface with arbitrary dielectric profiles for remote sensing of subsurface soil moisture. IEEE Trans. Geosci. Rem. Sens. 45(2), 349–366 (2007)
41. Khorashadi-Zadeh, V., et al.: Scattered fields of a 2D rectangular room composed of Cinder block walls using Floquet-Fourier series expansion. IEEE Trans. Antenn. Propag. 67(1), 390–399 (2019)

42. Achouri, K., Caloz, C.: Design, concepts, and applications of electromagnetic metasurfaces. J. Nanophotonics. 7(6), 1095–1116 (2018)
43. Khatami, M.S., et al.: Analysis of electromagnetic scattering from 2D curved metasurfaces using the extinction theorem and the Floquet expansion. In: Proceedings of the 28th Iranian Conference Electrical Engineering (ICEE), pp. 1–4, Tabriz (2020)
44. Balanis, C.A.: Advanced Engineering Electromagnetics, 2nd edn. 588. John Wiley and Sons Pub. USA (2012)

How to cite this article: Khatami MS, Dehmollaian M, Yousefi L. Analysis of wave scattering from 2D curved metasurfaces using Floquet and Fourier series expansions. *IET Microw. Antennas Propag.* 2021;15:981–994. https://doi.org/10.1049/mia2.12115

APPENDICES

Floquet coefficients

Using Equations (7b), (8b), (9b), and (10b), we can write,

$$\begin{bmatrix} a_n \\ \\ b_n \end{bmatrix} = \frac{\mathrm{j}}{2Lk_{0nz}} \sum_m \int_{x_0}^{x_0+L} \left[\sqrt{1+f'^2(x')} \left(\frac{\tau_m - \alpha_m}{\chi^{tt}_{mm}} - \left(\tau_m + \alpha_m\right)\frac{k_0^2}{4}\chi^{yy}_{ee} \right) + \mathrm{j}\tau_m \left(k_{nx} f'(x') + \begin{bmatrix} +1 \\ \\ -1 \end{bmatrix} k_{0nz} \right) \right] \times e^{\mathrm{j}\left(\left(k_{nx}-k_{mx}\right)x' + \begin{bmatrix} -1 \\ \\ +1 \end{bmatrix} k_{0nz} f(x') \right)} \mathrm{d}x', \tag{11.1a}$$

$$\begin{bmatrix} c_n \\ \\ d_n \end{bmatrix} = \frac{\mathrm{j}}{2Lk_{0nz}} \sum_m \int_{x_0}^{x_0+L} \left[\sqrt{1+f'^2(x')} \left(\frac{\kappa_m - \gamma_m}{\chi^{tt}_{ee}} - \left(\kappa_m + \gamma_m\right)\frac{k_0^2}{4}\chi^{yy}_{mm} \right) + \mathrm{j}\kappa_m \left(k_{nx} f'(x') + \begin{bmatrix} +1 \\ \\ -1 \end{bmatrix} k_{0nz} \right) \right] \times e^{\mathrm{j}(k_{nx}-k_{mx})x' + \begin{bmatrix} -1 \\ \\ +1 \end{bmatrix} k_{0nz} f(x'))} \mathrm{d}x', \tag{11.1b}$$

and

$$\begin{bmatrix} A_n \\ \\ B_n \end{bmatrix} = \frac{-\mathrm{j}}{2Lk_{1nz}} \sum_m \int_{x_0}^{x_0+L} \left[\sqrt{1+f'^2(x')} \left(\frac{\tau_m - \alpha_m}{\chi^{tt}_{mm}} + \left(\tau_m + \alpha_m\right)\frac{k_0^2}{4}\chi^{yy}_{ee} + \mathrm{j}\alpha_m \left(k_{nx} f'(x') + \begin{bmatrix} +1 \\ \\ -1 \end{bmatrix} k_{1nz} \right) \right) \right] \times e^{\mathrm{j}((k_{nx}-k_{mx})x' + \begin{bmatrix} -1 \\ \\ +1 \end{bmatrix} k_{1nz} f(x'))} \mathrm{d}x', \tag{11.2a}$$

$$\begin{bmatrix} C_n \\ \\ D_n \end{bmatrix} = \frac{-\mathrm{j}}{2Lk_{1nz}} \sum_m \int_{x_0}^{x_0+L} \left[\sqrt{1+f'^2(x')} \left(\frac{\kappa_m - \gamma_m}{\chi^{tt}_{ee}} + \left(\kappa_m + \gamma_m\right)\frac{k_0^2}{4}\chi^{yy}_{mm} + \mathrm{j}\gamma_m \left(k_{nx} f'(x') + \begin{bmatrix} +1 \\ \\ -1 \end{bmatrix} k_{1nz} \right) \right) \right] \times e^{\mathrm{j}((k_{nx}-k_{mx})x' + \begin{bmatrix} -1 \\ \\ +1 \end{bmatrix} k_{1nz} f(x'))} \mathrm{d}x'. \tag{11.2b}$$